Key Engineering Materials
ISSN: 1662-9795, Vol. 1047, pp 53-64

Submitted: 2025-12-18
Revised: 2026-02-13
Accepted: 2026-02-14
Online: 2026-04-13

Advanced Characterization of Flexible Auxetic Resin Lattice Structures Produced by Stereolithography

Stefano Belcuore[1,a], Stefano Pandini[1,b], Elisabetta Ceretti[1,c], Abdullah Al Maharbi[2,d], Mohammed M. Al-Hinaai[3,e] and Paola Ginestra[1,f*]

[1]Department of Mechanical and Industrial Engineering, University of Brescia, Via Branze 38, 25123, Brescia (BS), Italy

[2]Department of Engineering, German University of Technology in Oman (GUtech), Oman

[3]Department of Electrochemistry and Catalysis, College of Applied and Health Sciences, A 'Sharqiyah University, Oman

[a]s.belcuore@unibs.it, [b]stefano.pandini@unibs.it, [c]elisabetta.ceretti@unibs.it, [d]22-0872@student.gutech.edu.om, [e]Mohammed.alhinaai@asu.edu.om, [f*]paola.ginestra@unibs.it

Keywords: lattice structures, flexible resin, stereolithography.

Abstract. Lattice metamaterials with adjustable auxetic behavior are characterized by periodic configurations of interconnecting struts and nodes, allowing for precise control over their macroscopic mechanical properties. Different lattice configurations were examined, two-unit cell variants with varying void fractions were assembled into crystalline-inspired designs, specifically simple cubic and body-centered cubic. Using vat photopolymerization, fabrication was carried out using a transparent biomedical elastomeric resin that was chosen for its exceptional ductility and strain tolerance. The curing, crosslinking and thermal mechanical stability of the resin were examined using Fourier Transform Infrared Spectroscopy and Differential Scanning Calorimetry, before and after polymerization. In order to determine specific stiffness, specific yield strength, mechanical characterization involved quasi-static uniaxial compression testing. The effect of different aspects of the macroscopic structures was also observed, exploiting diverse possible applications. The combination of geometry and the behavior of the elastomeric material allowed the creation of lightweight structures that could support large reversible deformations that could be used in soft robotics and healthcare devices.

Introduction

Lattice structures constitute a class of engineered cellular materials composed of periodically repeated unit cells, whose ordered networks of struts and nodes [1,2] allow control [3] over structural behavior. By tailoring geometry, these structures can be designed to exhibit a wide spectrum of mechanical responses ranging from bistability [4] and tunable Poisson's ratio [5] to deformation regimes [6]. Some configurations can deliver unconventional effects as auxetic structures [7–9], suitable for many applications, filtration devices [10], biomedical scaffolding[11], energy absorption and soft robotic systems [12]. In this study, the design process of the metamaterials originates from the base unit-cell. The main process is the transformation of a cube into a cuboctahedral [13,14] configuration by rotating each square face around its centroidal axis, generating a continuous topological reorganization while maintaining face geometry and edge lengths. On this framework, a secondary transformation is introduced by obtaining circular voids in the center of each face [15]. This modification triggers a torsional shift toward an octahedral arrangement and causes the narrow wall between the voids to elastically buckle [16,17]. These walls act as compliant hinges that guide the coordinated rotation of square and triangular surfaces. The structure ultimately undergoes a symmetric global contraction, reducing its volume. In elastomeric photopolymer, this deformation is fully reversible, and a specific subset of these materials consists of photocurable elastomeric formulations, which undergo photopolymerization reactions compatible with stereolithography (SLA) [18]. Developments in additive manufacturing (AM) have markedly enhanced the capability to produce lattice structures with intricate geometries and precise dimensional control. In vat-

photopolymerization processes such as SLA, a narrowly focused UV laser beam scans the resin, triggering localized photopolymerization. This solidification pathway enables fine feature resolution and smooth surface finishes, although it typically requires longer fabrication times relative to faster AM techniques. This study aims to demonstrate how SLA, used in combination with transparent, flexible, and biocompatible polymeric materials, enables the fabrication of geometrically complex structures. The investigation first focuses on the chemical composition and intrinsic properties of the material, followed by an analysis of the mechanical behavior and response of the cellular metamaterials produced across multiple aspect ratios.

Materials and Methods

Design.

The base unit cell was modeled in Autodesk Inventor Professional (version 2025, ©1982–2025 Autodesk) to parametrize the geometry through three independent design variables. These parameters, the inscribed outer diameter, the inner pore diameter, and the inscribed angle, define the global dimensions of the unit cell and its porosity. Two different cell geometries were examined in this study, distinguished only by their void fraction. Cell "A" exhibits a higher density, whereas cell "B" is characterized by increased porosity and consequently lower density. The unit cells were assembled into two distinct lattice configurations: simple cubic (SC) and body-centered cubic (BCC). In this framework, the SC arrangement is generated from cell "A", while the BCC lattice is composed of cell "B". To further investigate structures with reduced aspect ratios (i.e., thickness to width ratio), an additional group of samples was produced by adding the prefix "1:4" to the nomenclature, corresponding to a thickness/width ≈ 0.4. This procedure yielded the 1:4 SC and 1:4 BCC structures, which maintain the same spatial organization as SC and BCC but incorporate modified geometric proportions. The geometries SC, 1:4 SC, BCC, 1:4 BCC are illustrated in Fig. 1C (i, iii) and Fig. 1D (i, iii) while in Fig. 1A (i) and Fig. 1B (i) are presented the unit cells employed in the lattices. The three parametric variables are inscribed angle, inner pore diameter and inscribed outer diameter and are detailed in Fig. 1A (iii) and Fig. 1B (iii). BCC and SC structures consist of a 3 × 3 × 3 array of unit cells, while 1:4 BCC consists of a 5×5×3 array of unit cells and 1:4 SC is made of 6x6x2, to ensure that the samples retain the same aspect ratio. The spatial configuration of the unit cells "A" and "B" is shown in Fig. 1C (ii) and Fig. 1D (ii).

Production.

All samples were produced using a SLA 3D printing system (Form 3BL, © Formlabs 2025, Boston, MA, USA) in conjunction with the flexible photopolymer material (Biomed Elastic 50A V1), as illustrated in Fig. 2. The printing parameters were defined within the Preform slicing software (© Formlabs 2025, Boston, MA, USA) and are reported in Table 1. The subsequent post-processing procedures of washing and curing are essential for achieving the required quality and functional performance of the printed components and are also summarized in Table 1.

Table 1. Process and post-process parameters for Formlabs 3BL Printer.

Layer height [mm]	Washing Time [min]	Curing Time [min]	Drying Temperature [°C]	Washing Solution
0,100	15,0	30	70,0	Isopropyl Alcohol

Chemical and thermal analysis.

Chemical and thermal analysis characterization of the prepared specimens include density measurements, viscosity evaluation, and thermal and spectroscopic analyses. Thermal behavior was investigated by differential scanning calorimetry (DSC), while chemical functionalities were assessed by Fourier-Transform Infrared Spectroscopy (FT-IR). Rheological properties and density of the uncured resin were also quantified to evaluate its flow behavior, recoating performance, and optical/mechanical implications during the printing process. Viscosity of the uncured resin was evaluated to characterize flow properties relevant to recoating dynamics and fine feature replication

during stereolithographic printing. Measurements were carried out using a rotational viscometer (Ametek brookfield, Middleboro, Massachusetts, USA). Density of the uncured resin was determined to assess factors influencing light penetration depth, buoyancy effects during layer formation, and interlayer adhesion. Measurements were performed using pycnometry (25°C) and oscillating U-tube densitometer DMA 35 (Anton Paar, Graz, Austria). FT-IR spectra were acquired on the uncured resin using a Bruker FT-IR Spectrometer (Bruker, Billerica, Massachusetts, USA) to identify characteristic functional groups and verify the chemical composition prior to photopolymerization. DSC tests were performed on slices (about 10 mg) sectioned from the printed specimens. Thermal scans were conducted using a DSC Q100 calorimeter (TA Instruments, New Castle, Delaware, USA). Each sample was subjected to a single heating cycle from −50 °C to 150 °C at a constant heating rate of 10 °C/min.

Dimensional accuracy Analysis.

After fabrication, all specimens were examined using an optical microscope (Quick Scope QS250Z, ©Mitutoyo, Sakado, Japan) to assess dimensional accuracy. Five critical geometric parameters were measured: Total length, Right and Left wall thickness, and internal pore diameter along both the X and Y axes, as illustrated in Fig. 1A (ii) and Fig. 1B (ii). For BCC and SC samples, measurements were acquired from three cells located along the main diagonal on each of two mutually perpendicular faces. For the 1:4 BCC and 1:4 SC structures, one cell per row was evaluated on two orthogonal faces. For each of the five measured dimensions, the mean value and standard deviation were subsequently calculated.

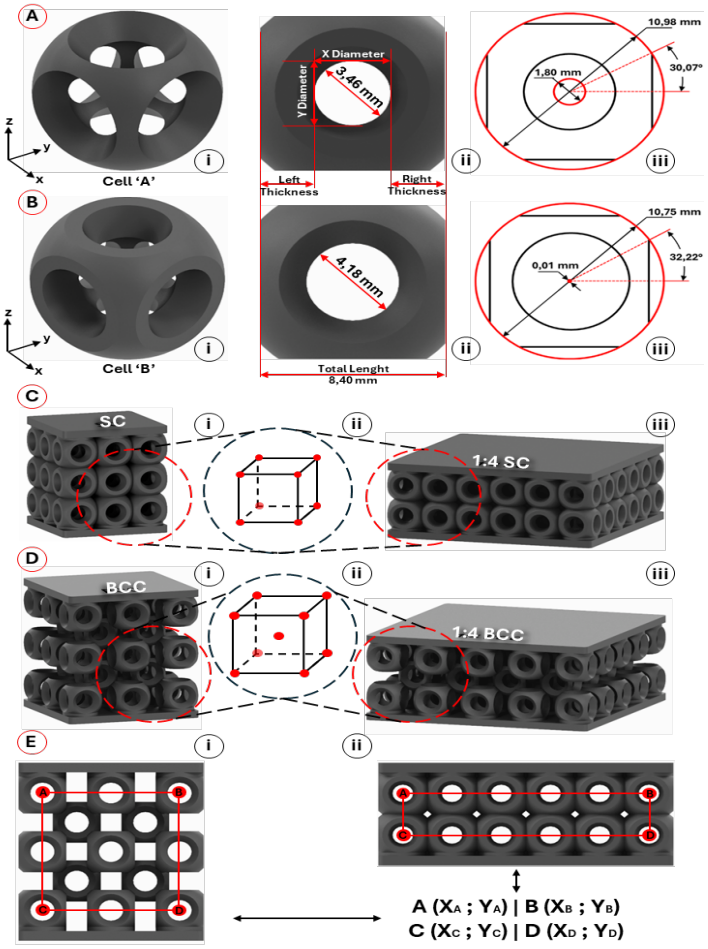

Fig. 1. Cell "A" and cell "B" are illustrated in A(i) and B(i). For both cell types, (ii) focus on the five critical parameters used to conduct the dimensional accuracy test, while (iii) display, highlighted in red, the three parametric values used to create the whole cell. C (i-iii) and D (i-iii) illustrate all the lattice structure and the spatial arrangement of the unit cells. E (i-ii) illustrates a schematic representation of the reference area used to calculate axial and transverse Poisson's ratio.

Compression test.

An electromechanical testing machine (Instron 3366, ©Instron, Norwood, Massachusetts, USA) equipped with a 10 kN load cell was employed to perform uniaxial compression experiments. Quasi static assessments were conducted under displacement controlled conditions and continued to high compression levels until structural failure typically manifested as the rupture of one or more cell walls or, for specimens that did not fracture (e.g., 1:4 SC configurations), until reaching the maximum applied load of 9000 N. Owing to variations in specimen height, a constant crosshead displacement rate was imposed to ensure an identical nominal strain rate (5 min^{-1}) across all tests. Throughout the uniaxial compression procedure, images were captured at fixed intervals of 10 seconds to document, frame by frame, the progression of deformation both along the loading axis and in the transverse direction, as well as the morphological evolution of the cellular architecture. The acquired images were subsequently processed using ImageJ (NIH, USA) to evaluate Poisson's ratio behavior of the structures. For this analysis, four tracking points were selected at the centers of the corner cells located along the structure's boundary, thereby defining a rectangular reference frame, as depicted in Fig. 1E (i, ii).

Results

All generated structures are shown in Fig. 2. Distinct differences among the structures are clearly observed, arising from the different spatial arrangements of the two cells, as well as from variations in aspect ratio and overall dimensions.

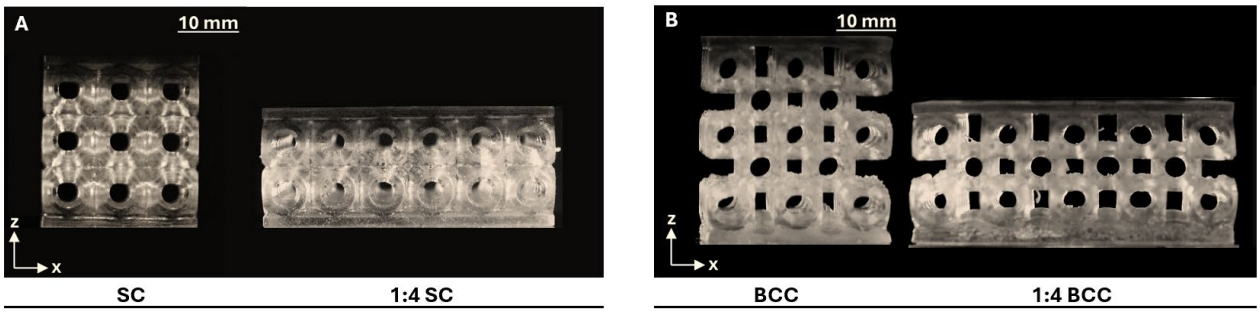

Fig. 2. Photographs of the fabricated samples produced using Biomed Elastic 50A resin and the Formlabs 3BL printer: (A) illustrate SC and 1:4 SC; (B) illustrate BCC and 1:4 BCC.

Chemical and thermal Analysis.

The study of the printed structures begins with an analysis of the chemical physical properties of the material. Table 2 summarizes the density and viscosity of the Biomed Elastic 50A (BE50A) resin. The viscosity of the resin, measured is 1120 mPa·s at 25 °C, plays a critical role in resin flow behavior and layer recoating during the printing process. A viscosity within the range of approximately 1000–1200 mPa·s ensures effective resin leveling between successive layers, which is particularly advantageous in both top-down and bottom-up SLA systems. Excessively high viscosity could impede smooth recoating and promote the entrapment of air bubbles, potentially leading to incomplete curing or interlayer delamination. Conversely, low viscosity could cause excessive resin drainage, resulting in reduced dimensional accuracy and poor feature definition. The moderately viscous nature of BE50A can support high resolution printing, especially for lattice-based or geometrically intricate structures, while enhancing process stability by minimizing motion-induced defects in uncured layers and improving surface finish. The density of the BE50A resin is equal to 1.13 g/cm³ at 25 °C, influences both optical penetration and curing behavior. This density indicates a material composition that allows sufficient ultraviolet light transmission, which is essential for achieving uniform curing depths and accurate resolution along the build direction. Significantly higher densities could increase light absorption or scattering, thereby compromising complete layer polymerization. From a structural perspective, a density of 1.13 g/cm³ provides a favorable mass-to-volume ratio, contributing to adequate mechanical integrity while limiting material consumption.

Moreover, this property enhances dimensional stability during post-curing, reducing the risk of shrinkage or warping, which is particularly critical for complex geometries.

Table 2. Chemical properties data of the printed structures material BE50A.

Property	Measured Value (25°C)	Unit	Method/ Instrumentation
Viscosity	1120	mPa*s	Rotational Viscosimeter
Density	1,13	g/cm^3	Pycnometry and Oscillating U-tube

The chemical characterization is further extended through FT-IR spectroscopy, which is a fundamental technique for confirming the chemical structure of the resin. FT-IR analysis enables the identification of characteristic vibrational modes, including carbonyl (C=O), ether/ester (C–O–C), and aliphatic C–H stretching regions. This analysis allows verification of the resin's primary polymer backbone, such as polylactic acid (PLA) based derivatives, assessment of functional groups responsible for UV-induced crosslinking, and detection of possible impurities or degradation products. The FT-IR spectrum, shown in Fig. 3, reveals a pronounced carbonyl stretching band around 1750 cm^{-1}, indicative of ester functional groups. This feature is essential for photopolymer resins, as ester groups play a key role in UV-activated crosslinking. The sharp and intense nature of this peak suggests a high degree of purity and an effective formulation of reactive PLA-based monomers or oligomers. In the 1080 cm^{-1} region, the presence of strong C–O–C stretching vibrations confirms the ester linkages connecting the PLA monomer units. These bonds are particularly responsive to UV exposure, enabling rapid and efficient polymerization under SLA conditions. Notably, the absence of broad O–H stretching bands in the 3200–3600 cm^{-1} range indicates low moisture content and a lack of unreacted acids or alcohols. This characteristic is advantageous for maintaining resin stability, ensuring consistent UV reactivity, and improving the dimensional accuracy of the printed components. Additionally, the observed aliphatic hydrocarbon stretching and bending modes, associated with –CH_3 and –CH_2 groups around 2945 cm^{-1} and 1450 cm^{-1}, reflect the flexible nature of the polymer chains. Such flexibility contributes to controlled shrinkage during curing and enhances the mechanical resilience of the final printed structures.

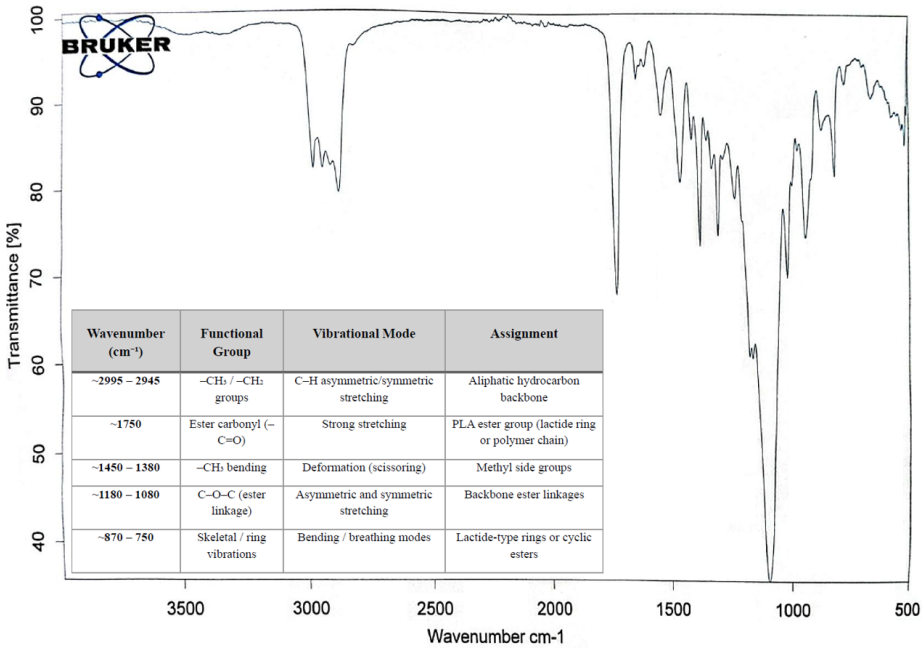

Fig. 3. FT-IR analysis performed on the resin in the liquid state prior to the crosslinking (curing) process.

Thermal analysis of the printed samples was carried out by differential scanning calorimetry (DSC), and the results are reported in Fig. 4. Specifically, Fig. 4A refers to a specimen extracted from the

BCC structure and a weak exothermic signal is observed during the first heating ramp, then it disappears during the second heating cycle. The same thermal behavior is consistently detected in all three specimens extracted from the SC structure, shown in Fig. 4B. This exothermic event can be attributed to the evaporation or release of residual solvents entrapped within the printed structures.

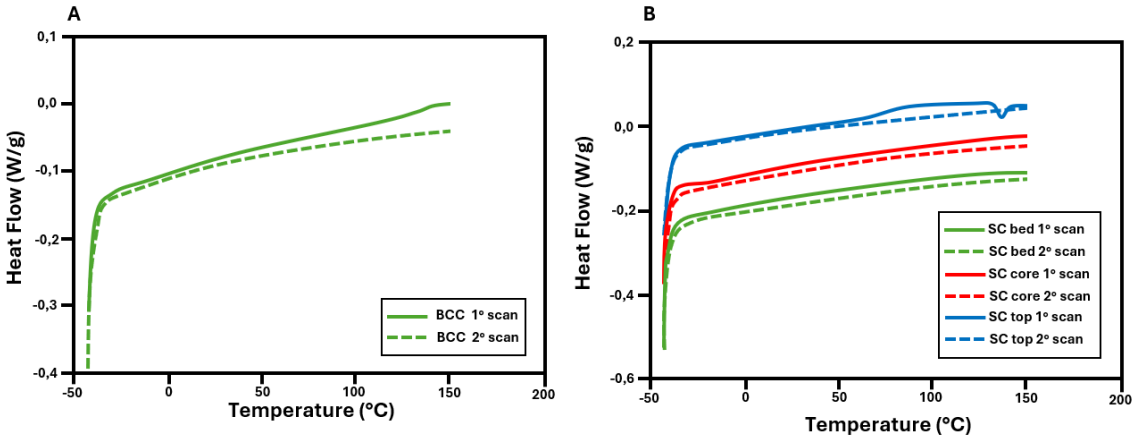

Fig. 4. DSC analysis performed on samples extracted from the structures. (A) shows the analysis carried out on a single sample taken from the BCC structure, whereas (B) presents the analysis performed on three different samples extracted from the SC structure: the layer in contact with the printing platform, the core, and the top layer.

Dimensional accuracy Analysis.

For each of the four fabricated structures, three primary target dimensions were defined, and measurements were performed on two faces of each specimen, as summarized in Table 3. The dimensional measurement results are presented as histograms in Fig. 5 and Fig. 6. Specifically, Fig. 5 reports the data for the BCC and SC structures, whereas Fig. 6 shows the results for the 1:4 BCC and 1:4 SC configurations. In all histograms, the error bars represent the standard deviation of the measured values, providing an indication of dimensional variability, while the horizontal red line denotes the nominal target dimension specified in the CAD model. BCC and SC structures were designed using different repeating unit cells and consequently their corresponding reference CAD target values are different.

Table 3. Dimensional accuracy analysis values for each structure Diameter (X and Y), Thickness (LH and RH) and total Length (L) are reported in Fig. 1 A,B (iii).

SAMPLE	CELL	SIDE	DIAMETER [mm]			THICKNESS [mm]			TOTAL LENGTH [mm]	
			CAD	X	Y	CAD	LH	RH	CAD	L
SC		Face 1	3,46	3,50 ± 0,04	3,24 ± 0,08	2,47	2,49 ± 0,03	2,48 ± 0,06	8,40	8,45 ± 0,07
		Face 2		3,48 ± 0,01	3,23 ± 0,07		2,50 ± 0,06	2,48 ± 0,02		8,45 ± 0,10
BCC		Face 1	4,18	4,32 ± 0,05	3,63 ± 0,29	2,11	2,00 ± 0,06	1,91 ± 0,11	8,40	8,20 ± 0,10
		Face 2		4,36 ± 0,02	3,75 ± 0,33		1,93 ± 0,04	1,93 ± 0,04		8,20 ± 0,07
1:4 SC		Face 1	3,46	3,56 ± 0,06	3,15 ± 0,16	2,47	2,34 ± 0,11	2,38 ± 0,08	8,40	8,25 ± 0,09
		Face 2		3,59 ± 0,05	3,13 ± 0,21		2,33 ± 0,20	2,39 ± 0,09		8,27 ± 0,15
1:4 BCC		Face 1	4,18	4,49 ± 0,10	3,93 ± 0,11	2,11	1,85 ± 0,08	1,87 ± 0,05	8,40	8,21 ± 0,06
		Face 2		4,43 ± 0,04	3,83 ± 0,40		1,89 ± 0,04	1,88 ± 0,07		8,19 ± 0,05

The graphs associated with the SC structure Fig. 5A are used as the reference case. Nonetheless, several relevant trends can be identified. As shown in Fig. 5A (i), the diameters measured along the horizontal (X) direction exhibit a higher mean value than those measured along the vertical (Y) direction. In addition, the X-axis measurements display a lower standard deviation and are in closer agreement with the nominal dimension defined in the CAD model. Notably, the results are consistent across the two analyzed faces, as both X and Y direction diameters show comparable values and trends. The largest deviation from the CAD reference is observed for the Y-axis diameters, with an average difference of -0.20 mm. From Fig. 5A (ii), it is evident that the left cell wall is systematically thicker than the right one. Among the two, the right wall thickness most closely matches the target value specified in the CAD model. The maximum deviation from the nominal dimension occurs for the left wall thickness, with a mean offset of +0.03 mm, indicating good dimensional stability and overall process consistency. The final graph Fig. 5A (iii) shows that the mean values are identical between the two measurement faces. However, this consistency is not fully reflected in the dispersion of the data, as the standard deviation is slightly higher for Face 2. In both cases, the largest deviation from the CAD reference corresponds to a mean offset of +0.05 mm. The dimensional analysis of the BCC metamaterial, reported in Fig. 5B, reveals trends that are shared with SC structure, while also highlighting distinct deviations associated with this specific structural configuration. As shown in Fig. 5B (i), the internal diameter measurements follow a pattern like SC structure; however, a systematic offset is observed along the horizontal (X) direction, where all measured values exceed the nominal dimension defined in the CAD model. This behavior results in the largest discrepancy with a maximum deviation of -0.50 mm relative to the target value. Fig. 5B (ii) presents the cell wall thickness measurements, which display relatively uniform mean values across the analyzed faces, despite noticeable differences in the associated standard deviations. In all cases, the measured thicknesses remain below the CAD reference, with a maximum deviation of -0.20 mm, indicating consistent under-sizing. The cell length results reported in Fig. 5B (iii) show identical mean values for both measurement faces, demonstrating good repeatability. Nevertheless, these mean values are significantly lower than the corresponding CAD specification when compared to SC structures. The maximum deviation from the nominal value in this case reaches 0.20 mm, confirming a systematic reduction in cell length.

Fig. 6A (i) exhibits the same behavior observed for the SC structure, with diameters measured along the horizontal (X) direction showing higher mean values than those measured along the vertical (Y) direction. Moreover, the X-axis measurements are characterized by a lower standard deviation and a closer agreement with the nominal dimensions defined in the CAD model. The results are consistent across the different analyzed faces, indicating good repeatability. Fig. 6A (ii) highlights a systematic trend in wall thickness measurements: the left-side thickness is consistently smaller than the right side thickness. Nevertheless, both values remain below the CAD reference, with a maximum deviation of -0.13 mm. Finally, Fig. 6A (iii) shows that the mean values measured on the two faces are very similar, demonstrating uniformity between measurement locations. However, both values deviate from the CAD specification, exhibiting an average offset of -0.15 mm. Fig. 6B (i), which reports the internal cell diameter, shows trends consistent with those observed in the previously analyzed structures. Conversely, Fig. 8B (ii) highlights a distinct behavior, as all mean values are closely clustered and exhibit a systematic deviation from the CAD reference of approximately -0.30 mm. Fig. 8B (iii) also presents tightly grouped average values, with a uniform offset of about −0.20 mm relative to the nominal dimensions defined in the CAD model.

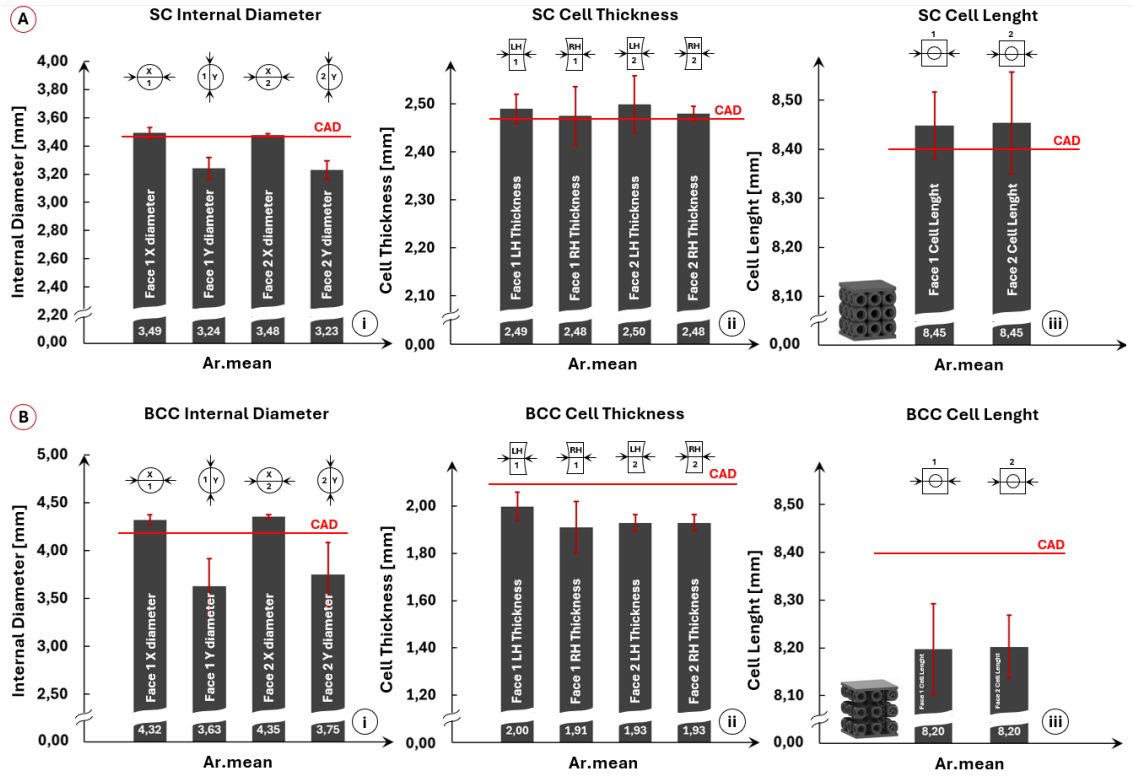

Fig. 5. Shows graphs related to the SC (A) and BCC (B) structures; each structure includes three analyses: internal cell diameter (i), cell thickness (ii), and cell length (iii). The columns represent the mean values, and error bars indicating the standard deviation. The horizontal red line denotes the CAD model reference value. Number "1" positioned on top of the columns refer to face 1, while number "2" correspond to face 2.

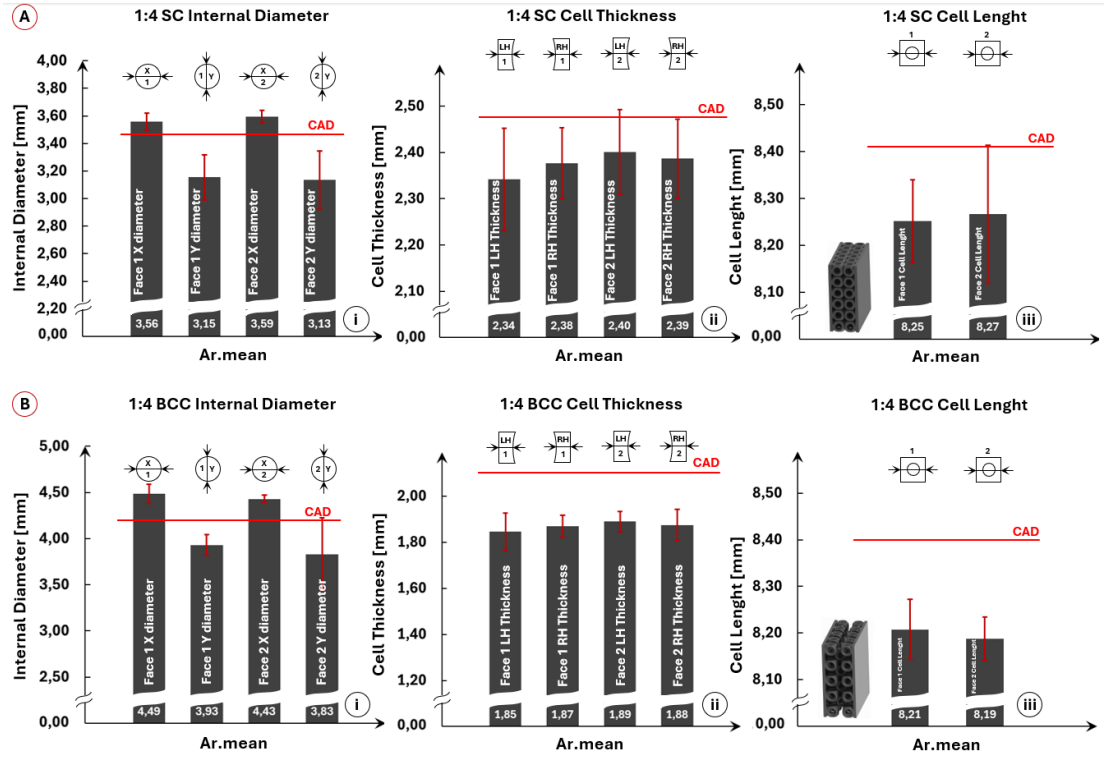

Fig. 6. Shows graphs related to the 1:4 SC (A) and 1:4 BCC (B) structures; each structure includes three analyses: internal cell diameter (i), cell thickness (ii), and cell length (iii). The columns represent the mean values, and error bars indicating the standard deviation. The horizontal red line denotes the CAD model reference value. Number "1" positioned on top of the columns refer to face 1, while number "2" correspond to face 2.

Compression test.

Fig. 7 presents the specific apparent stress versus apparent strain responses of the studied geometries, the term apparent is used to indicate that the stress was calculated as the applied force normalised by the total cross-sectional area, while the strain was evaluated as the ratio between the crosshead displacement and the initial specimen height, specific instead refers to normalization of the stress by the density of the lattice. A solid cube fabricated from Biomed Elastic 50A (BE50A) resin is included as a reference to represent the mechanical behavior of the bulk material and to emphasize the higher apparent compliance of the lattice-based samples. Curves reveals a progressive reduction in apparent stiffness, starting from 1:4 SC to 1:4 BCC, governed by both the relative density and the specific unit cell topology. The most important values are reported in Table 4, for each configuration, the density, specific apparent Young's modules, specific stress at a fixed apparent strain level (20%), and Poisson's ratio. The highest stiffness is achieved by the solid cube, with a specific apparent Young's modulus of 2.3 MPa/(g/cm^3). Among the lattice structures, the 1:4 SC and SC configuration exhibit the highest stiffness. The remaining systems show a more compliant mechanical response. Notably, these structures display a similar deformation behavior: an initial linear elastic region which ends one is reached a value of apparent strain occurring between 5% and 15%, then a pronounced stress plateau is observed which is subsequently followed by a rapidly specific apparent stress increase at higher deformations in the densification zone. The critical points highlighted in Fig.7 correspond to the onset of structural collapse, key feature for energy absorption applications. In contrast, the SC based structures do not exhibit a defined plateau; instead, only an inflection point is observed in the stress strain curves, indicating a change in slope associated with barreling effects. Under compressive loading, the SC and 1:4 SC structures show some barreling phenomena, characterized by an increase in lateral dimensions. Conversely, the BCC and 1:4 BCC configurations exhibit minimal lateral expansion and deform predominantly through localized buckling of the cell struts. These local instabilities progressively evolve into global deformation modes, resulting in complex collapse mechanisms distinct from those observed in the SC architectures.

Uniaxial compression tests also enabled the evaluation of Poisson's ratio, characterizing the transverse to axial strain response under compressive loading. The SC-based structures exhibit a progressive increase in transverse deformation during the initial stages of axial compression, corresponding to a positive Poisson's ratio. In contrast, the BCC-based structures display transverse strains fluctuating around zero and a slightly negative transverse strain can be observed. These behaviors correspond, respectively, to a positive Poisson's ratio for the SC structures and a negative Poisson's ratio for the BCC structures, which indicating an auxetic mechanical response.

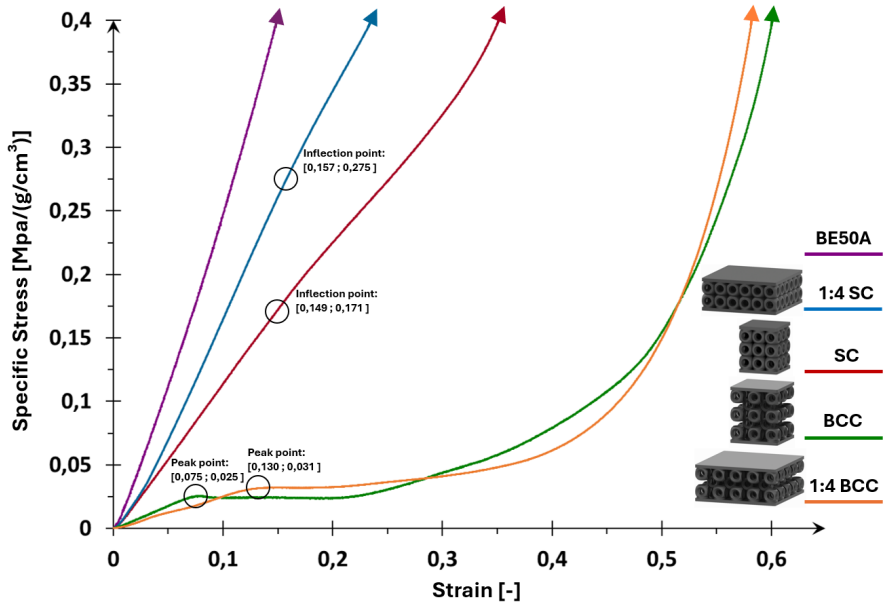

Fig. 7. Specific stress–strain curves of all the samples along with the BE50A curve (in purple) representing the resin.

Table 4. Mechanical properties data of the printed structures.

Structure	ρ [g/cm³]	E^I [MPa/(g/cm³)]	$\sigma_{0,2}$ [MPa/(g/cm³)]	$\nu_{0,2}$ [-]
BE50A	1,01	2,30	0,584	0,44
SC	0,58	1,12	0,225	0,14
BCC	0,30	0,34	0,024	-0,05
1:4 SC	0,63	1,55	0,340	0,20
1:4 BCC	0,36	0,24	0,032	-0,02

Discussion

Dimensional accuracy Analysis.

Cell A, as designed, exhibits higher resistance to stress during the printing process compared to Cell B. This improved mechanical response can be attributed to the different level of porosity. The lower effective porosity of Cell A results enhances its ability to withstand process-induced stresses during fabrication. Furthermore, the spatial arrangement of the SC cells provides additional structural stability throughout the manufacturing process, particularly during the progressive formation of the lattice. This enhanced stability is associated with the significant reduction of unsupported surfaces relative to the BCC spatial configuration. In the SC arrangement, the geometric continuity and connectivity between adjacent struts limit the extent of overhanging features, thereby reducing deformation during layer-by-layer solidification. The aspect ratio also exerted a detrimental influence on dimensional accuracy. Specifically, structures characterized by a lower aspect ratio exhibited a higher number of cells affected by dimensional discrepancies. Collectively, these three factors cooperate to define the measured overall dimensional accuracy.

Compression test.

The fundamental difference between structures characterized by an SC arrangement and those based on a BCC topology lies in their deformation mechanisms under compressive loading. SC structures exhibit an extended linear elastic region, beyond this regime, instabilities first develop locally in the form of cell barreling phenomena, where individual unit cells undergo progressive lateral expansion. As deformation proceeds, these localized instabilities evolve into a global mode involving the entire structure. In contrast, BCC structures display a shorter linear elastic region, followed by a distinct plateau phase in which deformation progresses at nearly constant stress. This stress plateau is associated with progressive cell collapse mechanisms. The deformation process culminates in a densification regime, where the collapsed cells compact and the stress rises rapidly due to material consolidation. The experimentally measured Poisson's ratio further highlights the different instability mechanisms between the two configurations. In BCC structures, a negative Poisson's ratio was observed during deformation, indicating auxetic behavior. This negative value implies localized densification mechanisms occurring during compression, which differ significantly from the lateral expansion typically observed in SC structures. The specific energy required for deformation, quantified as the area under the specific apparent stress versus apparent strain curves, is significantly lower for BCC structures compared to SC counterparts. Nevertheless, the ability of BCC architectures to undergo substantial deformation without a corresponding increase in stress, due to the extended plateau region, makes them particularly attractive for energy absorption applications.

Conclusion

The study focused on both the mechanical analysis of the structures and the characterization of the material from which they are composed. Chemical and thermochemical analyses revealed excellent properties for the fabrication of complex geometries, additionally confirming that the manufacturing process was carried out correctly. Dimensional analysis showed that the highest dimensional precision and accuracy are achieved in structures with an aspect ratio greater than unity and without

unsupported elements or large overhangs. Nevertheless, the deviations from the threshold values set in the CAD model remain limited and do not affect the overall mechanical behavior of the structures. Mechanical analysis highlights the wide range of mechanical properties that these structures can provide, enabling potential applications where higher compliance is preferred over high stiffness. Image acquisition during mechanical testing allowed the calculation of Poisson's ratio for each structure, to verify the presence of auxetic behavior. BCC structures exhibit this behavior, although only weakly, likely due to the presence of planar elements that inhibit the free movement of the upper and lower rows of cells.

References

[1] ISFA 2016 : International Symposium on Flexible Automation : August 1-3, 2016, Cleveland, Ohio. IEEE, 2016.

[2] C. Pan, Y. Han, and J. Lu, "Design and optimization of lattice structures: A review," Sep. 02, 2020, *MDPI AG*. doi: 10.3390/APP10186374.

[3] C. Coulais, E. Teomy, K. de Reus, Y. Shokef, and M. van Hecke, "Combinatorial Design of Textured Mechanical Metamaterials," Aug. 2016, doi: 10.1038/nature18960.

[4] A. Rafsanjani and D. Pasini, "Bistable auxetic mechanical metamaterials inspired by ancient geometric motifs," *Extreme Mech Lett*, vol. 9, pp. 291–296, Dec. 2016, doi: 10.1016/j.eml.2016.09.001.

[5] A. Clausen, F. Wang, J. S. Jensen, O. Sigmund, and J. A. Lewis, "Topology Optimized Architectures with Programmable Poisson's Ratio over Large Deformations," *Advanced Materials*, vol. 27, no. 37, pp. 5523–5527, Oct. 2015, doi: 10.1002/adma.201502485.

[6] A. Cutolo, S. Palumbo, A. R. Carotenuto, E. Sacco, and M. Fraldi, "A class of periodic lattices for tuning elastic instabilities," *Extreme Mech Lett*, vol. 55, p. 101839, Aug. 2022, doi: 10.1016/j.eml.2022.101839.

[7] R. Lakes, "Advances in negative Poisson's ratio materials," *Advanced Materials*, vol. 5, no. 4, pp. 293–296, Apr. 1993, doi: 10.1002/adma.19930050416.

[8] J. Zeng, H. Hu, and L. Zhou, "A study on negative Poisson's ratio effect of 3D auxetic orthogonal textile composites under compression," *Smart Mater Struct*, vol. 26, no. 6, May 2017, doi: 10.1088/1361-665X/aa6fe6.

[9] N. Pagliocca, K. Z. Uddin, I. A. Anni, C. Shen, G. Youssef, and B. Koohbor, "Flexible planar metamaterials with tunable Poisson's ratios," *Mater Des*, vol. 215, Mar. 2022, doi: 10.1016/j.matdes.2022.110446.

[10] H. M. A. Ali, M. Abdi, S. A. Zahedi, and Y. Sun, "Design of a programmable particle filtering medium using a novel auxetic metamaterial," *Smart Mater Struct*, vol. 32, no. 6, p. 064006, Jun. 2023, doi: 10.1088/1361-665X/acceea.

[11] X. Ren, J. Shen, P. Tran, T. D. Ngo, and Y. M. Xie, "Design and characterisation of a tuneable 3D buckling-induced auxetic metamaterial," *Mater Des*, vol. 139, pp. 336–342, Feb. 2018, doi: 10.1016/j.matdes.2017.11.025.

[12] A. Lazarus and P. M. Reis, "Soft Actuation of Structured Cylinders through Auxetic Behavior," *Adv Eng Mater*, vol. 17, no. 6, pp. 815–820, Jun. 2015, doi: 10.1002/adem.201400433.

[13] "SYNERGETICS Explorations in the Geometry of Thinking," 1997.

[14] A. D. Joseph Clinton, advanced structural geometry dies part geometric transformation concept for expanding rigid Structures," 1971.

[15] J. Shim, C. Perdigou, E. R. Chen, K. Bertoldi, P. M. Reis, and J. W. Hutchinson, “Buckling-induced encapsulation of structured elastic shells under pressure”, doi: 10.1073/pnas.111567410.

[16] C. Gao, V. Slesarenko, M. C. Boyce, S. Rudykh, and Y. Li, “Instability-Induced Pattern Transformation in Soft Metamaterial with Hexagonal Networks for Tunable Wave Propagation,” *Sci Rep*, vol. 8, no. 1, p. 11834, Aug. 2018, doi: 10.1038/s41598-018-30381-1.

[17] K. Bertoldi, M. C. Boyce, S. Deschanel, S. M. Prange, and T. Mullin, “Mechanics of deformation-triggered pattern transformations and superelastic behavior in periodic elastomeric structures,” *J Mech Phys Solids*, vol. 56, no. 8, pp. 2642–2668, Aug. 2008, doi: 10.1016/j.jmps.2008.03.006.

[18] Stefano Belcuore, Stefano Pandini, Elisabetta Ceretti, Paola Ginestra, Flexible resins lattices produced by stereolithography for biomedical applications, Materials Research Proceedings, Vol. 54, pp 12-21, 2025.